Tip effect and structural disordering in Bi_2WO_6 for enhanced piezo-photocatalytic nitrogen oxidation to nitric acid

Xiaoxu Deng [b,1], Peng Chen [c,1], Ruirui Cui [b], Weichao Huang [b], Yubo Wu [b], Xu Wang [b], Chaoyong Deng [a,b,*]

[a] *School of Electronics and Information Engineering, Guiyang University, Guiyang, Guizhou 550005, China*
[b] *Key Laboratory of Electronic Composites Materials of Guizhou Province, College of Big Data and Information Engineering, Guizhou University, Guiyang, Guizhou 550025, China*
[c] *Key Laboratory of Green Chemical and Clean Energy Technology of Guizhou Provincial, School of Chemistry and Chemical Engineering, Guizhou University, Guiyang, Guizhou 550025, China*

ABSTRACT

Piezo-photo coupling effect in charge separation has garnered substantial attention in recent research. However, the piezoelectricity-induced charges are inevitably depleted by the photoinduced current near the interface. Herein, we propose a meticulously designed conformity-directional dual electric field by introducing the tip effects and structural disordering in Bi_2WO_6. In the absence of cocatalysts, Bi and O vacancies rich Bi_2WO_6 with a Bi^0 cluster ($Bi^0/Bi_{2-x}WO_{6-x}$, BBW) exhibited remarkable piezo-photocatalytic nitrogen oxidation to nitric acid rates (5.26 mg g^{-1} h^{-1}), which is 5 times that of pure Bi_2WO_6. Theoretical and experimental results demonstrated that the cluster and vacancies acted as the major strain and potential center, which can be referred to as the "tip effect" and structural disordering that enhanced the piezoelectric-polarization electric field and the photoinduced built-in electric field along the same direction to promote charge transfer and exciton dissociation. Moreover, the cluster and vacancies acted as activation sites for O_2 and N_2, reducing the surface reaction barrier. Thus, the proposed method will aid in designing dual-polarization electric fields for enhancing carrier separation.

1. Introduction

As an essential chemical, nitric acid (HNO_3) has been widely applied in agriculture and industry [1]. Currently, the industrial production of HNO_3 primarily relies on the Ostwald and Haber–Bosch processes, resulting in considerable energy consumption and greenhouse gas emissions [2]. To address these concerns, the photocatalytic fixation of N_2 with O_2 for producing HNO_3 (NOR) presents an appealing strategy to leverage renewable energy sources and ambient conditions, offering a potential alternative for practical application [3]. However, the artificial photocatalytic NOR process using heterogeneous semiconductors poses substantial challenges, including inferior quantum efficiency, rapid electron recombination rates, and formidable dissociation energy with respect to the N≡N bond (940.95 kJ) [4]. Recently, piezoelectric catalysis has attracted considerable attention by relying on the mechanical stress applied to the materials for evaluating the charge separation efficiency [5–7]. Therefore, piezo-photocatalysis, wherein a

semiconductor is simultaneously exposed to light irradiation and mechanical stress, holds great potential for promoting NOR activity.

Currently, considerable attention is focused on noncentrosymmetric materials to enhance piezo-photocatalytic performance. To date, traditional noncentrosymmetric materials, such as $g-C_3N_4$, CdS, ZnO, $BaTiO_3$, $Bi_4Ti_3O_{12}$, and $PbTiO_3$, have been proposed for piezo-photocatalytic applications [8–11]. Bi_2WO_6, a representative member of the Aurivillius group, demonstrates considerable performance in photocatalysis owing to its suitable energy band and unique atomic structure [12]. Moreover, Bi_2WO_6 exhibits strong ferroelectric properties $P_r = 50$ μC cm^{-2}) owing to the coherent deviation of W atoms within the WO_6 octahedron [13,14]. However, the piezo-photocatalytic performance of pure Bi_2WO_6 is inadequate for industrial applications owing to the accumulation of normal dipole moments and spontaneous polarization predominantly along the c-axis, causing positive and negative charge centers to overlap [15]. To address this limitation, extensive efforts have been directed toward the development of ultrathin 2D nanostructures

---

with high anisotropy of polarization charges, aiming to reduce charge migration distances and facilitate charge transfer [16,17]. However, this approach remains challenging and fails to provide a comprehensive solution. Notably, defect engineering has emerged as a promising strategy for tailoring the electronic structures of semiconductors [18–20]. Wang et al. reported that oxygen vacancies considerably improve the piezo-photocatalytic degradation activity by promoting O_2 activation and polarization [21]. However, certain studies reported that monovacancies serve as electron and hole active sites, thereby restricting the improvement in photocatalytic performance [22]. Moreover, the migration of charges in monovacancies during piezocatalysis remains enigmatic. Thus, achieving a rational design of the inherent structure coupling piezoelectricity and photocatalysis presents a desirable yet challenging goal. Furthermore, elucidating the relationships between multimolecular reactions and atomic configurations is of utmost importance.

Herein, we employed a brief chemical reduction method to elaborate Bi and O vacancies rich Bi_2WO_6 with a Bi^0 cluster (referred to as Bi^0/ $Bi_{2-x}WO_{6-x}$ or BBW). Subsequently, we utilized the well-designed BBW catalyst to enhance piezo-photocatalytic NOR activity under mild conditions without using any sacrificial agents or cocatalysts. Remarkably, BBW achieved an outstanding NO_3^- formation rate (5.26 mg g^{-1} h^{-1}) and stability, which are 3.51 and 1.95 times that achieved solely under ultrasound and light illumination, respectively. Through a combination of theoretical simulations and experimental data, we elucidated that the cluster and vacancies acted as the major strain inducers and potential centers, a phenomenon referred to as the "tip effect." This effect enhanced the piezoelectric-polarization electric field and built-in electric field in the same direction, facilitating charge transfer and exciton dissociation. Furthermore, the presence of Bi^0 clusters and vacancies resulted in the activation of N_2 and O_2 species, respectively, preventing the undesired confusion of multimolecular activation. This study provides a comprehensive understanding of multimolecular activation and offers valuable insights into the design of piezo-photocatalysts.

2. Experimental section

2.1. Preparation of Bi_2MoO_6 with O vacancies (SBW)

A mixture of 0.329 g of Na_2WO_4·2 H_2O, 0.96 g of $Bi(NO_3)_3$·5 H_2O, and 0.05 g of cetyltrimethylammonium bromide (CTAB) was prepared in 80 mL of deionized water and stirred for 0.5 h. Subsequently, the resulting solution was transferred to a 100 mL Teflon-lined autoclave and heated at 120 °C for 24 h. The obtained SBW was subjected to washing, filtration, and drying steps to complete the synthesis process.

2.2. Preparation of Bi and O vacancies combined with Bi^0 containing Bi_2WO_6 (BBW)

To prepare the BBW catalyst, 0.5 g of SBW was dispersed in 50 mL of deionized water and subjected to ultrasonication for 0.5 h. Further, 0.02 g of $NaBH_4$ was added to the solution, followed by stirring for 6 h. The resulting BBW was collected after subsequent washing, filtration, and drying.

2.3. Preparation of Bi_2WO_6 (BW)

For the synthesis of bulk Bi_2WO_6, the same procedure as that for SBW was followed, except for the omission of CTAB from the reaction mixture.

3. Results and discussion

3.1. Characterizations of catalysts

The synthesis of Bi and O vacancies combined with Bi^0 in Bi_2WO_6 (BBW) was achieved using the solvothermal method, as depicted in Fig. 1a. As previously mentioned, the ultrathin Bi_2WO_6 with abundant O defects was prepared through a hydrothermal process employing a surface termination agent [23,24]. Notably, CTAB was utilized to bond to the surfaces of Bi_2WO_6, effectively covering the dangling bonds and creating numerous O vacancies [24]. Subsequently, a traditional reductant was employed to form Bi^0 nanoparticles in situ [25]. Consequently, Bi ions were extracted from the crystal lattice of Bi_2WO_6, resulting in the formation of Bi vacancies [26].

The morphology of BBW was characterized using scanning electron microscopy (SEM), transmission electron microscopy (TEM), and atomic force microscopy (AFM). As illustrated in Fig. 1b–c and S1 (Supporting Information, SI), all the prepared samples exhibited a nanosheet structure with an average breadth of 3–5 μm. The AFM images (Fig. S2, SI) revealed that these nanosheets had a thickness of approximately 8 nm. The lattice spacing fringes observed in Fig. 1d corresponded to a D-spacing of 0.259 nm, attributed to the (220) crystallographic plane of Bi_2WO_6 [27]. Furthermore, the lattice fringes of 0.328 nm and 0.227 nm could be assigned to the (012) and (110) planes of Bi, respectively [28], indicating the presence of metallic Bi on the surface of BBW. Notably, some nanoparticles were observed to be anchored on the nanosheet surface, providing further evidence of the presence of Bi tips within the nanosheets, facilitating charge transfer and spontaneous polarization. In Fig. 1f–h, the uniform dispersion of W, O, and Bi elements can be observed in the nanosheets. Moreover, BBW exhibited a relatively larger BET-specific surface area compared to SBW and BW (Fig. S3, SI), which is advantageous for light absorption and reactant transfer.

The structural crystallinity of the Bi_2WO_6 samples was assessed using X-ray diffraction (XRD). Fig. 2a displays characteristic peaks observed at 28.3°, 32.8°, 32.9°, 34.6°, 47.0°, 55.8°, 58.5°, 68.7°, 75.9°, and 78.5°, corresponding to the (131), (200), (002), (220), (260), (331), (262), (400), (193), and (204) crystallographic planes of Bi_2WO_6 (JCPDS 39–0256), respectively [29]. Additionally, small peaks are observed in BBW at 27.2°, 37.9°, and 39.8°, which align with the (012), (104), and (110) planes of metallic Bi (JCPDS 44–1246), respectively [30]. Notably, SBW exhibits a slight peak shift compared to BW, indicating the introduction of vacancies that can induce strain modification in the crystal lattice. In contrast, BBW demonstrates a shift toward higher angles, indicating an increased interplanar distance and crystal size of Bi_2WO_6 owing to the presence of Bi, implying disorder within the internal structure of BBW and potentially enhancing the piezoelectric potential. The Raman spectra shown in Fig. 2b exhibit distinct bands of BBW. The peaks at 706, 798, and 823 cm^{-1} correspond to the symmetric stretching vibration of W_2O_4, antisymmetric and symmetric A_g modes of terminal O–W–O groups, respectively [31]. Furthermore, the antisymmetric and symmetric peaks in BBW and SBW exhibit slight shifts toward higher wavenumbers compared to BW, indicating the presence of surface disorders and enhancing the polarization strength of Bi_2WO_6 [32, 33]. The considerable reduction in the peak intensity at 308 cm^{-1} can be attributed to the motions of Bi^{3+} and WO_6^{6-}, highlighting the strong interaction between metallic Bi and Bi_2WO_6 [34,35]. Notably, BBW displays an evident band shift at 150 cm^{-1}, indicating partial oxygen loss in Bi_2WO_6 [36], thus indicating the presence of high surface disorder.

X-ray photoelectron spectroscopy (XPS) was utilized to investigate the surface chemical composition and chemical states of BBW. Fig. 2c exhibits two peaks at 164.7 eV and 159.3 eV, corresponding to Bi 4 $f_{5/2}$ and Bi 4 $f_{7/2}$ of Bi^{3+}, respectively, in pure Bi_2WO_6 [36]. Notably, two additional peaks are observed in BBW at 157.6 eV and 162.9 eV, indicating the presence of Bi^0. The molar ratio of metallic Bi species to the total Bi 4 f peaks is 2.5 %. As shown in Fig. 2d, the peaks at 36.8 and 34.6 eV are attributed to W 4 $f_{5/2}$ and W 4 $f_{7/2}$, respectively, in BBW [37]. The peaks at 530.6, 530.4, and 529.3 eV correspond to the oxygen vacancy, W–O, and Bi–O bonds in BBW, respectively (Fig. 2e). Compared to pure Bi_2WO_6, the Bi 4 f, W 4 f, and O 1 s peaks in SBW exhibit a shift toward lower binding energy, indicating the presence of
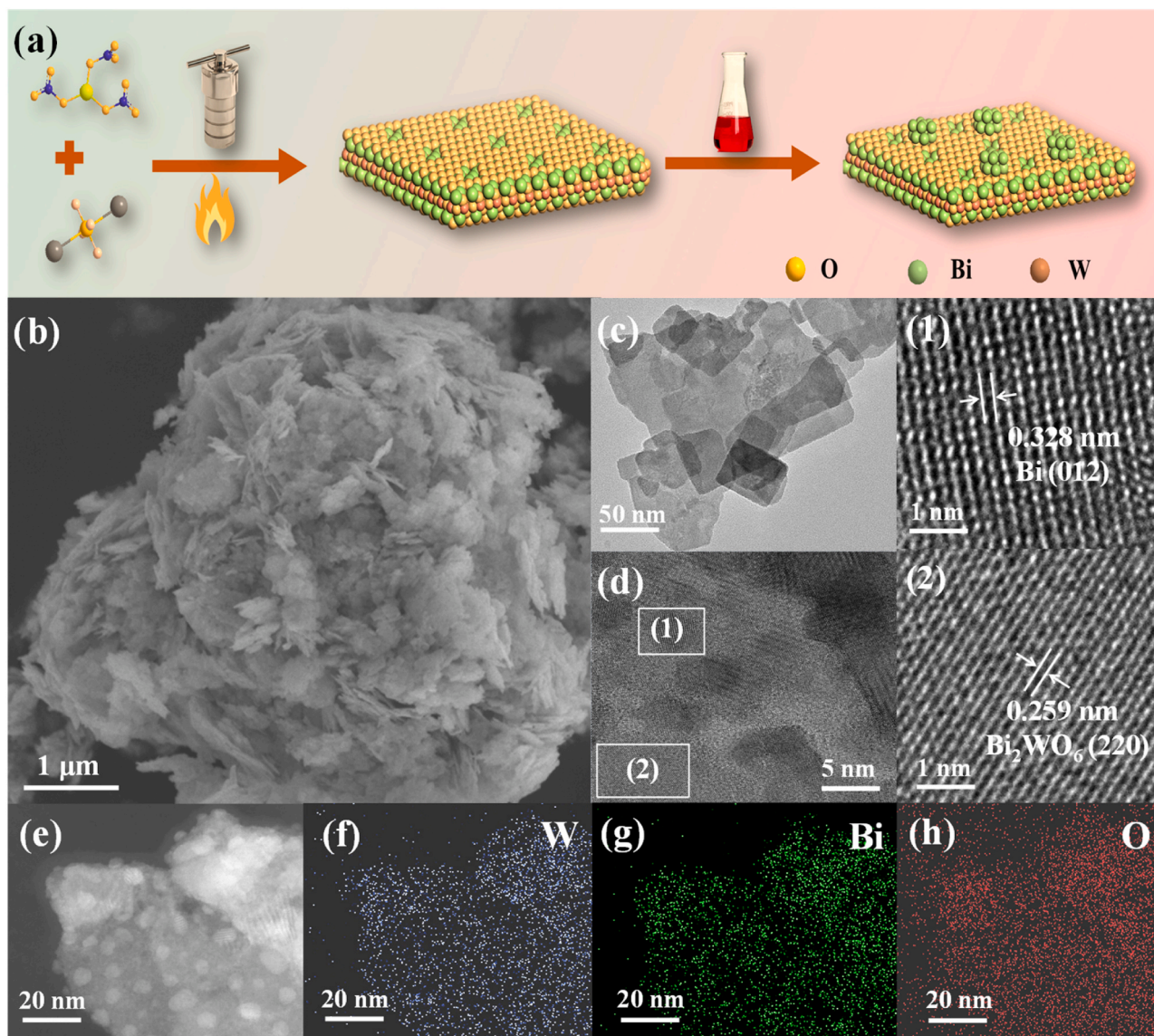
Fig. 1. (a) Schematic of the synthesis method. (b) SEM, (c–e) TEM, and (f–h) corresponding mapping images of BBW.

oxygen vacancies [38]. Moreover, a negative shift is observed in BBW compared to SBW, indicating additional surface disorder caused by the formation of Bi^0. To further investigate the surface disorder, electron paramagnetic resonance (EPR) spectroscopy was conducted. Fig. 2f displays a high EPR signal at g = 2.003 in SBW and BBW, confirming the presence of oxygen vacancies in the materials [39]. Moreover, the EPR signal at g = 2.14 is caused due to Bi surface defects [40]. This indicates that the formation of Bi^0 can disrupt the surface structure of Bi_2WO_6 and enhance polarization. Furthermore, inductively coupled plasma–optical emission spectroscopy (ICP-OES) was employed to confirm the composition of the composites. As listed in Table S1, the molar ratio of Bi to Mo in BW, SBW, and BBW is 1.91, 1.85, and 1.83, respectively, demonstrating the presence of bismuth and oxygen vacancies in BBW. Thus, all the spectral analysis results confirmed the proposed detailed structure.

3.2. Analysis of photo-piezoelectric properties

The light absorption capability of the prepared samples was measured using ultraviolet–visible (UV–vis) diffuse reflectance spectroscopy. As shown in Fig. S4a (SI), the absorption edge of BW exists at 450 nm. With the introduction of vacancies, the absorption edge of SBW

exhibits a red shift, accompanied by an increase in absorbance. Furthermore, a tail of 400–800 nm is observed for BBW, which is attributed to the surface plasmon resonance of Bi nanoparticles in Bi_2WO_6. This confirms that the introduction of vacancies and the presence of metallic elements enhance the light absorption capacity. The band gap values of BW, SBW, and BBW are estimated to be 2.49, 2.29, and 1.71 eV, respectively (Fig. S4c, SI). The valence band (VB) edges of BW, SBW, and BBW are measured to be 1.75, 1.67, and 1.70 eV, respectively (Fig. S4c, SI). Accordingly, the conduction band (CB) positions for BW, SBW, and BBW are estimated to be − 0.01, − 0.62, and − 0.74 eV, respectively (Fig. S4d, SI), indicating the thermodynamic capacity of the prepared samples to oxidize N_2 into NO_3^- (the equilibrium potential of N_2/NO is 1.67 eV) [41]. Additionally, the CB level of the samples was estimated using Mott-Schottky (M-S) plots (Fig. S5, SI). The CB values were determined to be − 0.01, − 0.62, and − 0.74 eV for BW, SBW, and BBW, respectively, in line with UPS measurements. To gain insight into the enhanced light absorption of BBW, density functional theory (DFT) simulations were performed. Fig. S6a (SI) shows that the CB edge in BW primarily comprises the O 2p orbital, and the VB edge comprises the O 2p, Bi 6p, and W 4d orbitals. For SBW and BBW, a new defect level near the Fermi level is observed (Fig. S6b and c, SI),
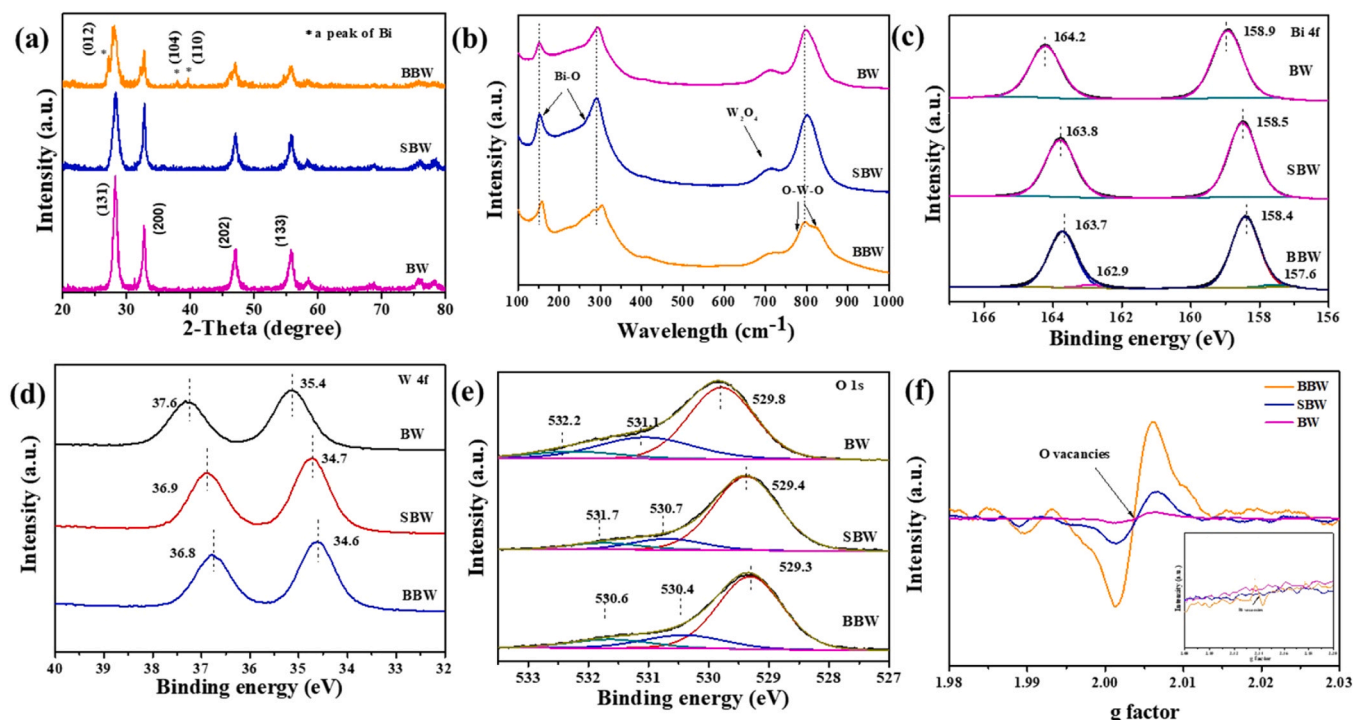
Fig. 2. (a) XRD patterns of the as-prepared samples. (b) Raman spectra of as-obtained samples. XPS spectra of (c) Bi 4 f, (d) W 4 f, and (e) O 1 s for prepared samples. (f) EPR spectra of BBW, SBW, and BW.

indicating a reduction in the required photoenergy for electron excitation and charge transfer [42]. Moreover, BBW exhibits a shallow energy level near the bottom of the CB compared to that of SBW, indicating that the introduction of Bi^0 and vacancies narrows the bandgap, enhancing the light absorption of Bi_2WO_6.

The piezoelectric properties of the prepared samples were evaluated using piezoelectric force microscopy (PFM). As shown in Fig. 3a–c, the relative amplitude image and phase image are consistent with the topographic image, indicating the high piezoelectricity of BBW. However, the PFM images of SBW and BBW gradually become less distinct (Fig. S7, SI), confirming that the presence of oxygen vacancies and metallic Bi enhances the piezoelectric potential. Fig. 3d–e and S8 (SI) show well-defined hysteretic amplitude-voltage curves under an alternating current voltage for all the prepared samples, indicating inherent ferroelectric properties. Furthermore, BBW (173 pm V^{-1}) exhibits a relatively higher maximum effective piezoelectric coefficient (d_{33}) compared to SBW (125 pm V^{-1}) and BW (95 pm V^{-1}), demonstrating that the introduction of vacancies and metallic elements enhances the piezoresponse of Bi_2WO_6.

To gain insights into the enhanced photo-piezoelectric properties of BBW, DFT, and piezoelectric simulations were performed. The charge density distribution is shown in Figs. S9–S11 (SI), displaying a balanced distribution of charges in BW. Notably, a negatively charged region is observed in the oxygen-vacancy center and Bi^0, while a positive charge is located in the Bi-vacancy center, indicating an unbalanced charge distribution that leads to the formation of the largest dipole moment. To investigate the polarity of the prepared samples, polarization electric field (P-E) measurements were conducted. Fig. S12 (SI) displays the remnant polarization of the prepared samples in the order of BBW > SBW > BW, indicating that the introduction of Bi^0 and vacancies promotes local polarization in Bi_2WO_6. To investigate the correlation between the structure and the piezoelectric effect, COMSOL Multiphysics was utilized for simulation. The simulated dimensions and polar axis of Bi_2WO_6 were set to $60 \times 60 \times 2$ nm^3 and subjected to a pressure of 10^3 Pa along the z-axis. As shown in Fig. S13 (SI), the piezoelectric potential difference of BW is 400 mV. After introducing some surface

clusters and holes, the maximum piezoelectric potential increased to 500 mV. Moreover, the clusters and holes acted as major strain and potential centers (Fig. 3h–i and S13–S14, SI), referred to as the "tip effect" that enhances the piezoelectric-polarization electric field. Thus, the results demonstrate that structural disordering and the tip effect enhance light absorption and local polarization as well as serve as strain centers to enhance the electric field.

3.3. Analysis of charge transfer for structural disordering and tip effect

As anticipated, the introduction of mechanical stress in photocatalysis can generate a considerable built-in electric field that promotes charge separation and transfer [43]. The built-in electric field is known to be influenced by two main factors: surface charge density and Zeta potential [44]. The Zeta potential of BBW was measured to be − 49.16 mV, which is 1.55 and 2.48 times higher than those of SBW and BW (Fig. 4d and S15, SI). The surface charge density was determined using AFM with a Kelvin probe. As shown in Fig. 4b and S16, the surface potential of BBW in the dark is 20.72 mV, which is 1.45 and 1.80 times higher than those of SBW and BW, indicating that the introduction of Bi^0 and vacancies contributes to a considerable built-in electric field that enhances charge separation and exciton dissociation. The surface potential of BBW increases to 24.42 mV under illumination (Fig. 4a). This trend is consistent with the results depicted in Fig. 4d and S16 (SI), indicating that the synergistic effect of mechanical stress and photocatalysis enhances the built-in electric field. Therefore, it can be concluded that the piezoelectricity-induced electric field is consistent with photocatalysis.

Based on DFT calculations and experimental results, the charge transfer in BBW can be elucidated. Fig. S17 (SI) shows that the work functions of BW, SBW, and BBW are 5.59, 4.38, and 3.62 eV, respectively, indicating that the introduction of Bi^0 and vacancies realigns the surface charge density of Bi_2WO_6. Based on these results, it can be inferred that electrons and holes spontaneously diffuse from Bi_2WO_6 to Bi^0 and Bi vacancies, establishing a new equilibrium state. Furthermore, COMSOL calculations confirmed that the high and lower potential
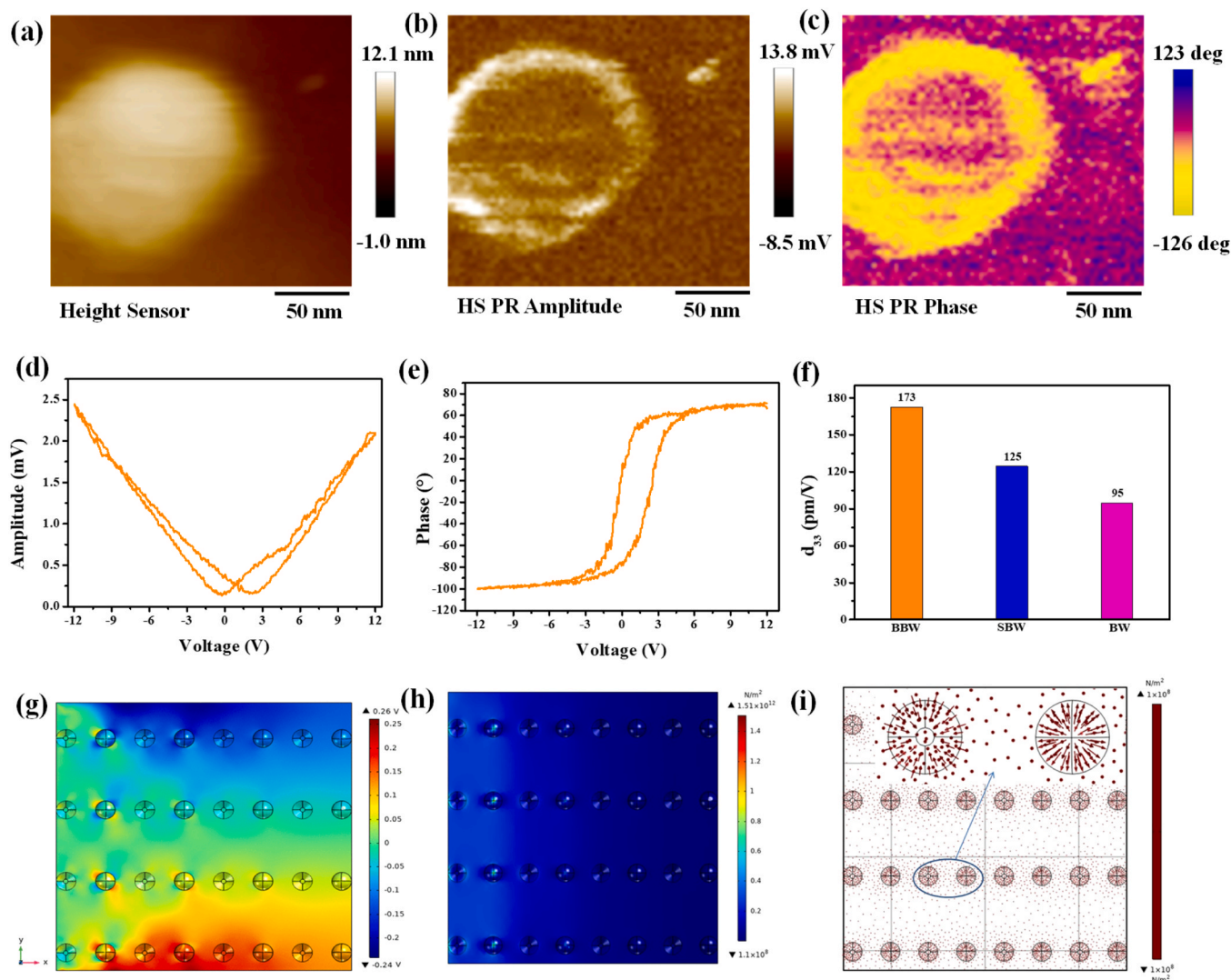
Fig. 3. PFM image of BBW (a) topography image, (b) amplitude image, and (c) phase image. (d) Piezoresponse amplitude butterfly loops and (e) phase hysteresis loops of BBW. (f) Maximum effective piezoelectric coefficient of as-prepared samples. COMSOL simulates the calculation of (g) piezoelectric potential and (h, i) stress distribution for BBW.

electric fields are located at the panel and cluster, respectively, supporting the charge transfer from the panel to the cluster. Thus, the tip effect and structural disordering induce a double electric field, including the piezoelectricity-induced electric field and the photo-generated built-in electric field in the same direction, thereby promoting charge transfer and exciton dissociation.

Excitonic effects play a crucial role in separating photoinduced charges by regulating Coulomb interactions. To gain a deeper understanding of the influence of excitonic effects, photoluminescence (PL) spectra and time-resolved transient PL decay spectra were analyzed. Fig. S18 (SI) shows a significant reduction in PL intensity for BBW and SBW compared to BW, indicating that the introduction of vacancies and Bi^0 greatly decreases the number of singlet excitons. As presented in Fig. 4e and Table S3 (SI), the average exciton lifetimes for BBW, SBW, and BW were 0.39, 0.66, and 0.78 ns, respectively. To further assess the thermodynamic capacity for exciton dissociation, temperature-dependent photoinduced luminescence was conducted. As shown in Fig. 4f and S19 (SI), the simulated exciton binding energies for BBW, SBW, and BW were 137, 363, and 476 meV, respectively. Therefore, it is evident that the introduction of vacancies and Bi considerably reduces the excitonic effect and enhances the population of charges in Bi_2WO_6.

To uncover the underlying mechanism of charge transfer in Bi_2WO_6,

transient current response and electrochemical impedance spectroscopy (EIS) experiments were performed. Fig. S20a (SI) displays the photocurrent response in the order of BBW > SBW > BW, indicating the highly inhibited recombination of charges through the introduction of vacancies and Bi. Notably, BBW exhibits the smallest semicircle radius (Fig. S21a, SI), indicating effective interfacial charge transfer and carrier separation. Furthermore, the introduction of vacancies and Bi^0 enhances the piezo-current densities (Fig. S20b, SI), consistent with the EIS results displayed in Fig. S21b (SI). As shown in Fig. 4g and S20c, BBW exhibits the highest piezo-photocurrent response, 2.43 and 3.76 times higher than the photocurrent and piezo-induced current intensity, respectively. In contrast, SBW and BW do not exhibit such differences (Fig. 4h), which aligns with the EIS results (Fig. S21c). Therefore, it can be concluded that the piezo-induced electric field and photoinduced electric field positively contribute to enhancing carrier separation (Fig. 4i).

3.4. Catalytic activity performance

In general, HNO_3 is an essential chemical widely used in agriculture and industry. In this study, the photocatalytic NOR activity of the as-prepared Bi_2WO_6 was evaluated under visible light illumination. In an Ar atmosphere or the absence of light illumination, O_2 and/or
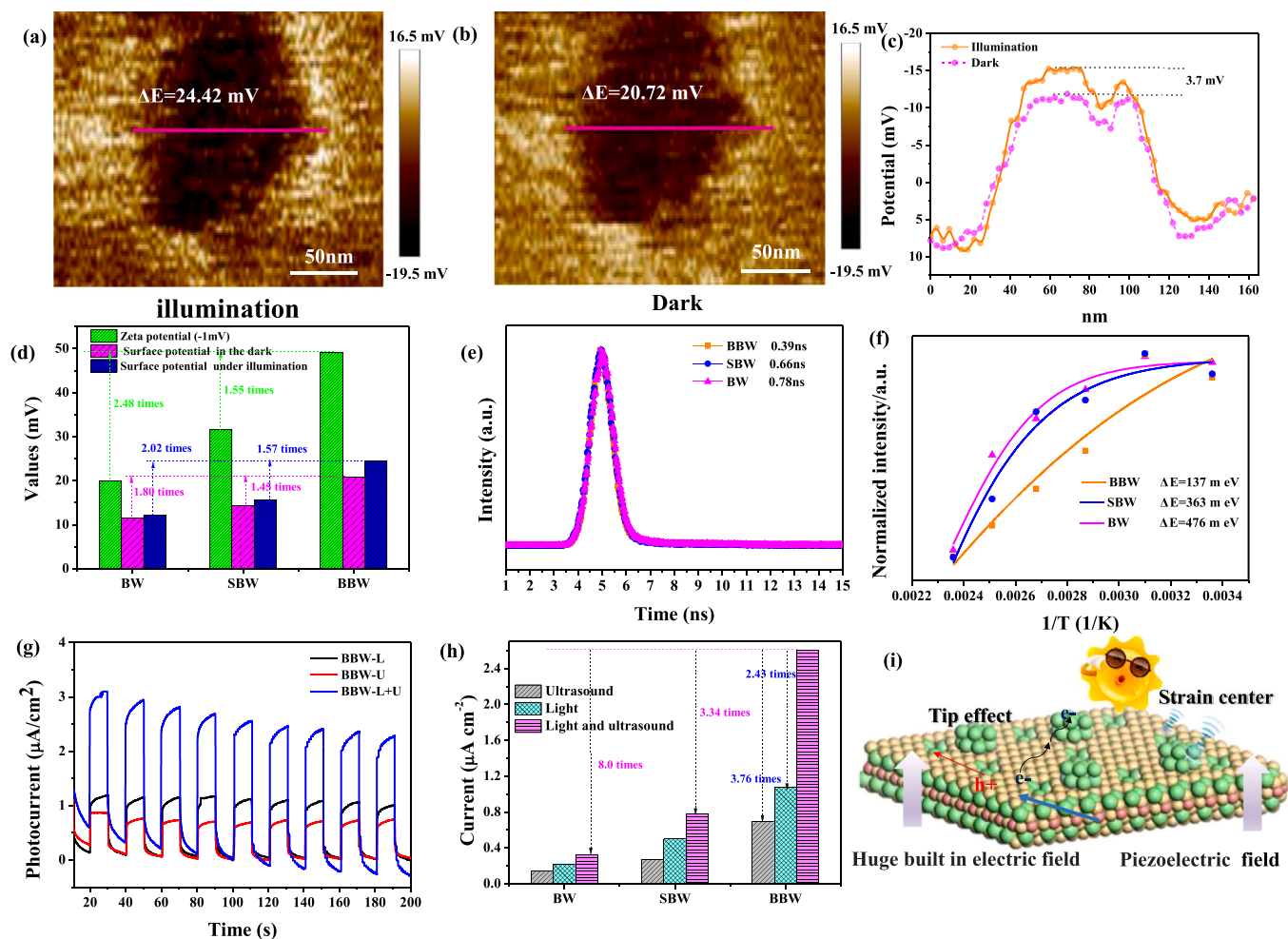
Fig. 4. KPFM potential images of BBW (a) under illumination and (b) in the dark. (c) Corresponding surface potential of BBW. (d) Characterization of the built-in electric field, (e) time-resolved transient PL (TRPL) decay, and (f) temperature-dependent luminescence of as-prepared samples. (g) Current density responses of BBW under various conditions. (h) Current density comparison of as-prepared samples under different conditions. (i) Schematic of the photo-piezocatalytic current process.

photocatalyst, no product was observed, confirming that O_2 and N_2 are prerequisite conditions for the photocatalytic reaction. As shown in Fig. 5a, the HNO_3 yields of BBW, SBW, and BW reached 2.70, 1.87, and 1.01 mg g^{-1} h^{-1}, respectively. Notably, BBW exhibited superior NOR values compared to SBW, BW, and previously reported results (table S4). Furthermore, the apparent quantum efficiency reached 0.148 at 400 nm. To further investigate the origin of HNO_3, an isotopic $^{15}N_2$ labeling experiment was conducted, providing credible results that demonstrated the N element in HNO_3 originated from N_2. Moreover, the cycling stabilities of BBW samples were examined, and as shown in Fig. S22a (SI), the performance of BBW was well-maintained, indicating its high stability.

To further enhance the photocatalytic NOR performance, the synergy effect of piezo-photocatalysis was investigated. Under ultrasonic vibration, the HNO_3 evolution rates of BBW, SBW, and BW were 1.50, 0.95, and 0.28 mg·g^{-1} h^{-1}, respectively, indicating that the vacancies and metal elements could enhance the piezoresponse of Bi_2WO_6. However, under the coupling effect of ultrasound and light without the use of a sacrificial reagent or cocatalyst, the HNO_3 formation rate of BBW increased considerably to 5.26 mg·g^{-1}·h^{-1}, which is 3.51 and 1.95 times higher compared to those achieved only under ultrasound or light illumination, respectively. Moreover, the HNO_3 formation rates of SBW and BW under the coupling effect of ultrasound and light were 2.13 and 1.51 mg·g^{-1} h^{-1}, respectively, representing only 1.13 and 1.50 times that of under light illumination. This enhancement can be attributed to

the introduction of vacancies and Bi, which induce a tip effect and structural disordering, thereby enhancing the polarity and built-in electric field of Bi_2WO_6, which remarkably promotes charge transfer and the synergistic effect of piezo-photocatalytic performance. Importantly, BBW exhibited outstanding stability based on repeated experiments (Figs. S22–S24, SI). In summary, BBW proves to be a promising candidate for NOR under the synergistic effect of ultrasound and light conditions.

3.5. Mechanism analysis

The NOR reaction involves the activation of multiple molecules, including N_2, O_2, and H_2O. Therefore, in addition to water contact angle measurements, we conducted temperature-programmed adsorption of N_2 and O_2. As shown in Figs. S25–27 (SI), the highest variations in the chemical adsorption temperature and water contact angle occurred for O_2 and N_2, indicating the contribution of Bi^0 and vacancies toward the activation of reactants. Although BBW exhibited excellent chemical adsorption temperatures for O_2, N_2, and water, the multicomponent nature of the reaction induced competitive adsorption for active sites. To elucidate the catalytic mechanism of NOR at the molecular level, DFT calculations were performed. Based on the previous discussion on electron transfer, the Bi^0 sites were identified as the reduction centers. Thus, the free adsorption energies of O_2, N_2, and H_2O on the Bi^0 sites were calculated. As shown in Fig. 6a, the free adsorption energy of O_2
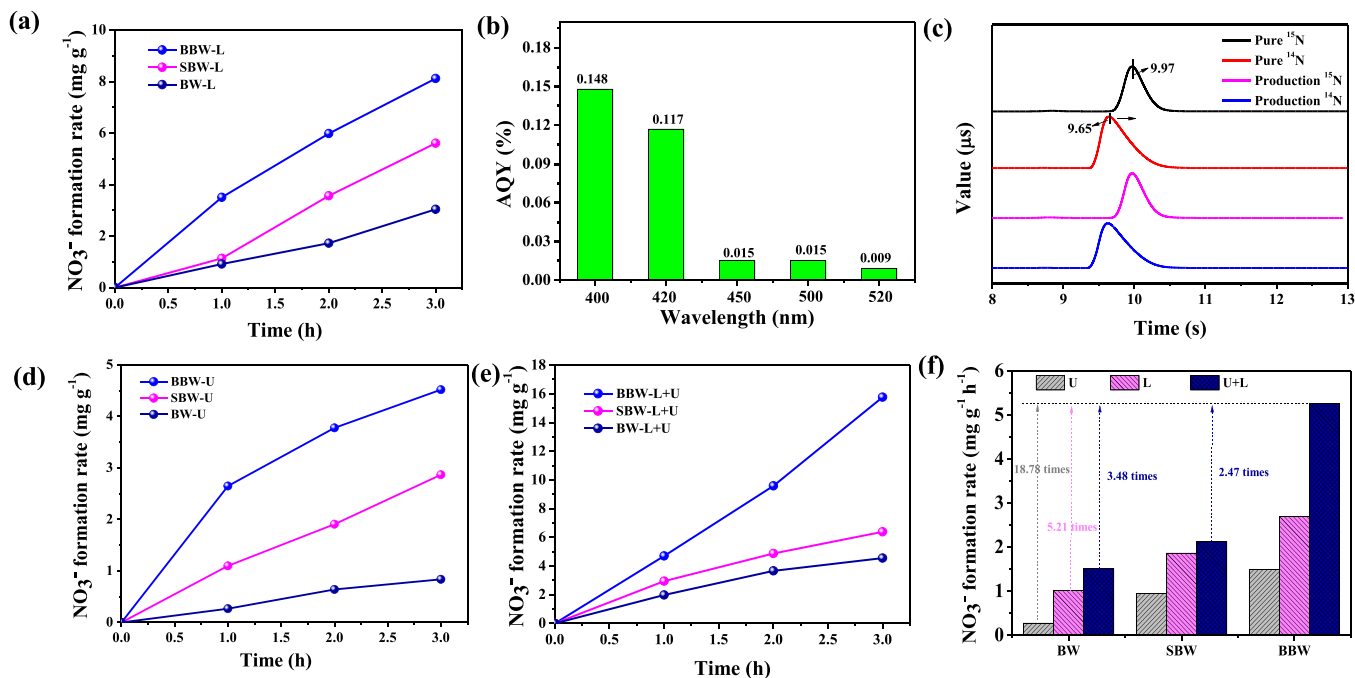
Fig. 5. (a) Photocatalytic NO_3^- yields over as-prepared samples. (b) The apparent quantum efficiency of BBW. (c) ^{15}N isotope tracing results over BBW. NO_3^- production rates over as-prepared samples under (d) ultrasound and (e) simultaneous light and ultrasonic irradiation. (f) NO_3^- formation rates under varying conditions.
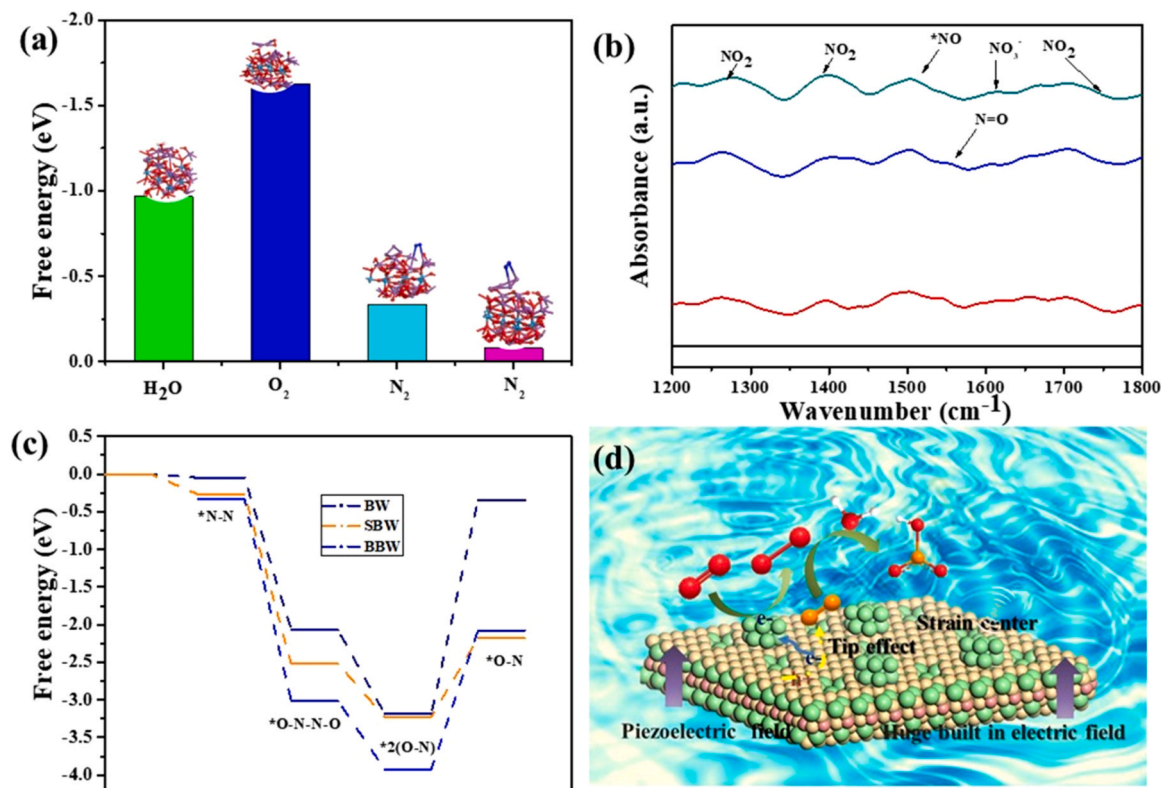

Fig. 6. (a) Adsorption energies of N_2, O_2, and H_2O on various sites of BBW. (b) In situ FT-IR spectra for catalytic nitrogen oxidation to nitric acid over BBW. (c) Gibbs free energy for the nitrogen oxidation to nitric acid progress over BBW. (d) Proposed process for piezo-photocatalytic nitrogen oxidation to nitric acid using BBW.

was higher compared to that of N_2 and water, indicating a higher priority for O_2 activation. Moreover, Bi^0 and Bi vacancies acted as active sites for O_2 and N_2, respectively. Furthermore, a better understanding of oxygen species was obtained through free radical quenching

experiments [45]. As shown in Fig. S28 (SI), the HNO_3 yield decreased considerably with the addition of *p*-benzoquinone, confirming that the N_2 oxidation process could proceed via the pathway where oxygen reacts with electrons to form superoxide radical ($O_2 \cdot^-$).

To further comprehend the NOR mechanism, in situ diffuse reflectance infrared Fourier transform spectroscopy was performed. As shown in Fig. 6b, the three peaks at 1257, 1440, and 1716 cm^{-1} were assigned to NO_2 species [46]. Moreover, the peaks at 1518, 1554, and 1624 cm^{-1} were ascribed to NO, N = O, and HNO_3 species, respectively [47]. These results indicate that NO and NO_2 serve as intermediates in the transformation of N_2 into HNO_3. Based on the DFT results, the catalytic reaction was simulated. As shown in Fig. 6b–c and S29, the adsorption energy for N_2 and O_2 occurred on the Bi vacancies and Bi^0 sites. The step of *N–N transforming into *NO–NO was identified as the major barrier in the NOR process. Therefore, the formation of HNO_3 through the reaction between N_2, O_2, and water may follow the reaction steps shown in Fig. S30.

Based on the aforementioned results and DFT simulation, a plausible reaction mechanism for NOR over BBW is proposed (Fig. 6d). Under light irradiation and ultrasonic vibration, electrons and holes are excited by BBW. Subsequently, these electrons and holes are selectively transferred to the Bi vacancies and Bi^0 sites, respectively, facilitated by the strong polarized electric field. The electrons can reduce O_2 to generate·O^{2-}, which eventually reacts with the adsorbed N_2 molecules and holes to form NO_x. Finally, HNO_3 is obtained through the reaction between NO_x, O_2, and water.

4. Conclusions

In conclusion, Bi and O vacancies combined with BBW were successfully prepared using a simple chemical reduction method. The optimized catalysts exhibited outstanding NO_3^- formation rates (5.26 mg g^{-1} h^{-1}) and stability under the combined effect of ultrasound and light, without the need for sacrificial reagents or cocatalysts. This performance is 3.51 and 1.95 times higher than those observed under ultrasound or light illumination alone, respectively. DFT calculations and experimental results demonstrated that the introduction of vacancies and Bi induced tip effects and structural disordering, enhancing the polarity and built-in electric field of Bi_2WO_6. This further promotes charge transfer and enhances the synergistic effect of piezo-photocatalytic performance. Moreover, the Bi vacancies and Bi^0 sites contribute to the activation of N_2 and O_2 species. Additionally, the significant role of superoxide radicals in the NOR reaction was confirmed. This study indicates the importance of vacancies and metal elements in piezo-photocatalysis and provides a deeper understanding of NOR reactions.

CRediT authorship contribution statement

Xiaoxu Deng: Conceptualization, Methodology, Investigation, Data curation, Writing-review & editing. **Peng Chen:** Conceptualization, Methodology, Data curation. **Ruirui Cui:** Methodology. **Weichao Huang:** Formal analysis. **Yubo Wu:** Methodology. **Xu Wang:** Supervision, Investigation. **Chaoyong Deng:** Conceptualization, Supervision, Re-Writing-review & editing, Funding acquisition.

Declaration of Competing Interest

The authors declare that they have no known competing financial interests or personal relationships that could have appeared to influence the work reported in this paper.

Data Availability

Data will be made available on request.

Acknowledgements

Appendix A. Supporting information

Supplementary data associated with this article can be found in the online version at doi:10.1016/j.apcatb.2023.123148.

References

[1] Y. Wang, T. Li, Y. Yu, B. Zhang, electrochemical synthesis of nitric acid from nitrogen oxidation, Angew. Chem. Int. Ed. 61 (12) (2022), e202115409.

[2] J.G. Chen, R.M. Crooks, L.C. Seefeldt, K.L. Bren, R.M. Bullock, M.Y. Darensbourg, P.L. Holland, B. Hoffman, M.J. Janik, A.K. Jones, M.G. Kanatzidis, P. King, K. M. Lancaster, S.V. Lymar, P. Pfromm, W.F. Schneider, R.R. Schrock, Beyond fossil fuel-driven nitrogen transformations, Science 360 (6391) (2018) eaar6611.

[3] Y. Liu, M. Cheng, Z. He, B. Gu, C. Xiao, T. Zhou, Z. Guo, J. Liu, H. He, B. Ye, B. Pan, Y. Xie, Pothole-rich ultrathin WO_3 nanosheets that trigger N—N bond activation of nitrogen for direct nitrate photosynthesis, Angew. Chem. Int. Ed. 58 (3) (2019) 731–735.

[4] L. Shi, Y. Yin, S. Wang, H. Sun, Rational catalyst design for N_2 reduction under ambient conditions: strategies toward enhanced conversion efficiency, ACS Catal. 10 (12) (2020) 6870–6899.

[5] L. Xu, L. Liu, Piezo-photocatalytic fuel cell with atomic Fe@MoS2 on CFC helical electrode has enhanced peroxymonosulfate activation, pollutant degradation and power generation, Appl. Catal. B: Environ. 304 (2022), 120953.

[6] S. Tu, Y. Guo, Y. Zhang, C. Hu, T. Zhang, T. Ma, H. Huang, Piezocatalysis and piezo-photocatalysis: catalysts classification and modification strategy, reaction mechanism, and practical application, Adv. Funct. Mater. 30 (48) (2020), 2005158.

[7] R. Su, Z. Wang, L. Zhu, Y. Pan, D. Zhang, H. Wen, Z.-D. Luo, L. Li, F.-t Li, M. Wu, L. He, P. Sharma, J. Seidel, Angew. Chem. Int. Ed, 60, 2021, p. 16019.

[8] R. Tang, D. Gong, Y. Zhou, Y. Deng, C. Feng, S. Xiong, Y. Huang, G. Peng, L. Li, Z. Zhou, Unique g-C_3N_4/PDI-g-C_3N_4 homojunction with synergistic piezo-photocatalytic effect for aquatic contaminant control and H_2O_2 generation under visible light, Appl. Catal. B: Environ. 303 (2022), 120929.

[9] X. Huang, R. Lei, J. Yuan, F. Gao, C. Jiang, W. Feng, J. Zhuang, P. Liu, Insight into the piezo-photo coupling effect of $PbTiO_3$/CdS composites for piezo-photocatalytic hydrogen production, Appl. Catal. B: Environ. 282 (2021), 119586.

[10] Q. Tang, J. Wu, X.-Z. Chen, R. Sanchis-Gual, A. Veciana, C. Franco, D. Kim, I. Surin, J. Pérez-Ramírez, M. Mattera, A. Terzopoulou, N. Qin, M. Vukomanovic, B. J. Nelson, J. Puigmartí-Luis, S. Pané, Tuning oxygen vacancies in $Bi_4Ti_3O_{12}$ nanosheets to boost piezo-photocatalytic activity, Nano Energy 108 (2023), 108202.

[11] C. Wang, F. Chen, C. Hu, T. Ma, Y. Zhang, H. Huang, Efficient piezocatalytic H_2O_2 production of atomic-level thickness $Bi_4Ti_3O_{12}$ nanosheets with surface oxygen vacancy, Chem. Eng. J. 431 (2022), 133930.

[12] C. Lu, X. Li, Q. Wu, J. Li, L. Wen, Y. Dai, B. Huang, B. Li, Z. Lou, Constructing surface plasmon resonance on Bi_2WO_6 to boost high-selective CO_2 reduction for methane, ACS Nano 15 (2) (2021) 3529–3539.

[13] Z. Kang, E. Lin, N. Qin, J. Wu, B. Yuan, D. Bao, Effect of oxygen vacancies and crystal symmetry on piezocatalytic properties of Bi_2WO_6 ferroelectric nanosheets for wastewater decontamination, Environ. Sci. Nano 8 (5) (2021) 1376–1388.

[14] J. You, Z. Liu, Z. Guo, M. Ruan, W. Yan, Doping of W Ions to modulate the polarization intensity of Bi_2WO_6 for efficient piezoelectric–photoelechochemical water splitting, ACS Appl. Energy Mater. 5 (9) (2022) 11472–11482.

[15] J. Yuan, X. Huang, L. Zhang, F. Gao, R. Lei, C. Jiang, W. Feng, P. Liu, Tuning piezoelectric field for optimizing the coupling effect of piezo-photocatalysis, Appl. Catal. B: Environ. 278 (2020), 119291.

[16] Z. Kang, N. Qin, E. Lin, J. Wu, B. Yuan, D. Bao, Effect of Bi_2WO_6 nanosheets on the ultrasonic degradation of organic dyes: roles of adsorption and piezocatalysis, J. Clean. Prod. 261 (2020), 121125.

[17] C. Hu, F. Chen, Y. Wang, N. Tian, T. Ma, Y. Zhang, H. Huang, Exceptional cocatalyst-free photo-enhanced piezocatalytic hydrogen evolution of carbon nitride nanosheets from strong in-plane polarization, Adv. Mater. 33 (24) (2021), e2101751.

[18] Y.C. Wang, J.M. Wu, Effect of controlled oxygen vacancy on H_2-production through the piezocatalysis and piezophototronics of ferroelectric R_3C $ZnSnO_3$ nanowires, Adv. Funct. Mater. 30 (5) (2019), 1907619.

[19] P. Wang, X. Li, S. Fan, Z. Yin, L. Wang, M.O. Tadé, S. Liu, Piezotronic effect and oxygen vacancies boosted photocatalysis C–N coupling of benzylamine, Nano Energy 83 (2021), 105831.

[20] Z. Kang, E. Lin, N. Qin, J. Wu, D. Bao, Bismuth vacancy-mediated quantum dot precipitation to trigger efficient piezocatalytic activity of Bi_2WO_6 nanosheets, ACS Appl. Mater. Interf. 14 (9) (2022) 11375–11387.

[21] P. Wang, X. Li, S. Fan, X. Chen, M. Qin, D. Long, M.O. Tadé, S. Liu, Impact of oxygen vacancy occupancy on piezo-catalytic activity of $BaTiO_3$ nanobelt, Appl. Catal. B: Environ. 279 (2020), 119340.

[22] M. Lyu, Y. Liu, Y. Zhi, C. Xiao, B. Gu, X. Hua, S. Fan, Y. Lin, W. Bai, W. Tong, Y. Zou, B. Pan, B. Ye, Y. Xie, Electric-field-driven dual vacancies evolution in ultrathin nanosheets realizing reversible semiconductor to half-metal transition, J. Am. Chem. Soc. 137 (47) (2015) 15043–15048.

[23] Y. Zhou, Y. Zhang, M. Lin, J. Long, Z. Zhang, H. Lin, J.C. Wu, X. Wang, Monolayered Bi_2WO_6 nanosheets mimicking heterojunction interface with open surfaces for photocatalysis, Nat. Commun. 6 (2015) 8340.

[24] Z. Xing, J. Hu, M. Ma, H. Lin, Y. An, Z. Liu, Y. Zhang, J. Li, S. Yang, From one to two: In situ construction of an ultrathin ^2D–^2D closely bonded heterojunction from a single-phase monolayer nanosheet, J. Am. Chem. Soc. 141 (2019) 19715.

[25] Y. Sun, Z. Zhao, W. Zhang, C. Gao, Y. Zhang, F. Dong, Plasmonic Bi metal as cocatalyst and photocatalyst: The case of $Bi/(BiO)_2CO_3$ and Bi particles, J. Colloid Inter. Sci. 485 (2017) 1–10.

[26] J. Wang, W. Wang, J. Wang, K. Xue, Y. Peng, Y. Yan, Y. Wang, H. Wang, Y. Wu, The generation of lattice oxygen defects enhanced by β particles: Layered microsphere-like Bi_2WO_6 as a template leads to $Bi_x@Bi_{2-x}WO_n$ for the efficient removal of oxytetracycline, Chem. Eng. J. 416 (2021), 129197.

[27] J. Wei, Y. Xia, A. Qayum, X. Jiao, D. Chen, T. Wang, Unexpected photoinduced room temperature magnetization in Bi_2WO_6 nanosheets, Small 16 (50) (2020), e2005704.

[28] H. Wang, D. Wei, Y. He, H. Deng, B. Wu, L. Yan, H. Gang, Y. Cao, L. Jin, L. Zhang, Carbon nanoarchitectonics with Bi nanoparticle encapsulation for improved electrochemical deionization performance, ACS Appl. Mater. Inter. 14 (11) (2022) 13177–13185.

[29] A. Hao, X. Ning, Y. Cao, J. Xie, D. Jia, Boosting the piezocatalytic performance of Bi_2WO_6 nanosheets towards the degradation of organic pollutants, Mater. Chem. Front. 4 (7) (2020) 2096–2102.

[30] L. Zhang, Z. Wang, C. Hu, B. Shi, Enhanced photocatalytic performance by the synergy of Bi vacancies and Bi^0 in Bi^0-$Bi_{2-δ}MoO_6$, Appl. Catal. B: Environ. 257 (2019) 117785.

[31] S. Liu, C. Wang, J. Wu, B. Tian, Y. Sun, Y. Lv, Z. Mu, Y. Sun, X. Li, F. Wang, Y. Wang, L. Tang, P. Wang, Y. Li, M. Ding, Efficient CO_2 electroreduction with a monolayer Bi_2WO_6 through a metallic intermediate surface state, ACS Catal. 11 (20) (2021) 12476–12484.

[32] Z. Wang, L. Zhang, X. Zhang, C. Hu, L. Wang, B. Shi, X. Cao, Enhanced photocatalytic destruction of pollutants by surface W vacancies in V_W-Bi_2WO_6 under visible light, J. Colloid Interf. Sci. 576 (2020) 385–393.

[33] Z. Kang, E. Lin, N. Qin, J. Wu, D. Bao, Bismuth vacancy-mediated quantum dot precipitation to trigger efficient piezoelectric activity of Bi_2WO_6 nanosheets, ACS Appl. Mater. Interf. 14 (9) (2022) 11375–11387.

[34] J. Jin, J. Sun, K. Lv, X. Guo, Q. Hou, J. Liu, J. Wang, Y. Bai, X. Huang, Oxygen vacancy BiO_{2-x}/Bi_2WO_6 synchronous coupling with Bi metal for phenol removal via visible and near-infrared light irradiation, J. Colloid Interf. Sci. 605 (2022) 342–353.

[35] Y. Huang, S. Kang, Y. Yang, H. Qin, Z. Ni, S. Yang, X. Li, Facile synthesis of Bi/ Bi_2WO_6 nanocomposite with enhanced photocatalytic activity under visible light, Appl. Catal. B: Environ. 196 (2016) 89–99.

[36] X. Li, F. Li, X. Lu, S. Zuo, C. Yao, C. Ni, Development of $Bi_2W_{1-x}Mo_xO_6$/ Montmorillonite nanocomposite as efficient catalyst for photocatalytic desulfurization, J. Alloy. Compd. 709 (2017) 285–292.

[37] Y. Zhang, Y. Li, Y. Yuan, Carbon quantum dot-decorated $BiOBr/Bi_2WO_6$ photocatalytic micromotor for environmental remediation and DFT calculation, ACS Catal. 12 (22) (2022) 13897–13909.

[38] D. Peng, H. Zeng, J. Xiong, F. Liu, L. Wang, S. Xu, Z. Yang, S. Liu, Tuning oxygen vacancy in Bi_2WO_6 by heteroatom doping for enhanced photooxidation-reduction properties, J. Colloid Interf. Sci. 629 (2022) 133–146.

[39] Y. Zhang, S. Gu, X. Zhou, K. Gao, K. Sun, D. Wu, J. Xia, X. Wang, Boosted photocatalytic nitrogen fixation by bismuth and oxygen vacancies in Bi_2MoO_6/ BiOBr composite structures, Catal. Sci. Technol. 11 (14) (2021) 4783–4792.

[40] Y. Teng, F. Teng, Investigation on surface metal vacancy electrochemistry, Electrochim. Acta 244 (2017) 1–7.

[41] W. Ren, Z. Mei, S. Zheng, S. Li, Y. Zhu, J. Zheng, Y. Lin, H. Chen, M. Gu, F. Pan, Wavelength-dependent solar N_2 fixation into ammonia and nitrate in pure water, Research 2020 (2020), 3750314.

[42] H. Xu, Y. Hu, D. Huang, Y. Lin, W. Zhao, Y. Huang, S. Zhang, Y. Tong, Glucose-induced formation of oxygen vacancy and Bi-metal comodified Bi_5O_7Br nanotubes for efficient performance photocatalysis, ACS Sustain. Chem. Eng. 7 (6) (2019) 5784–5791.

[43] X. Zhou, B. Shen, A. Lyubartsev, J. Zhai, N. Hedin, Semiconducting piezoelectric heterostructures for piezo- and piezophotocatalysis, Nano Energy 96 (2022), 107141.

[44] G. Zhang, Y. Xu, D. Yan, C. He, Y. Li, X. Ren, P. Zhang, H. Mi, Construction of K^+ ion gradient in crystalline carbon nitride to accelerate exciton dissociation and charge separation for visible light H_2 production, ACS Catal. 11 (12) (2021) 6995.

[45] M. Song, X. Deng, G. Li, Q. Wang, H. Peng, P. Chen, S.-F. Yin, Edge- and bridge-engineering-mediated exciton dissociation and charge separation in carbon nitride to boost photocatalytic H_2 evolution integrated with selective amine oxidation, J. Mater. Chem. A 10 (31) (2022) 16448–16456.

[46] T. Li, S. Han, C. Wang, Y. Huang, Y. Wang, Y. Yu, B. Zhang, Ru-doped Pd nanoparticles for nitrogen electrooxidation to nitrate, ACS Catal. 11 (22) (2021) 14032–14037.

[47] T. Li, S. Han, C. Cheng, Y. Wang, X. Du, Y. Yu, B. Zhang, Sulfate-enabled nitrate synthesis from nitrogen electrooxidation on a rhodium, Angew. Chem. Int. Ed. 61 (26) (2022), e202204541.